

Excluded volume effects on tangentially driven active ring polymers

A. Lamura^{1,*}

¹*Istituto Applicazioni Calcolo, Consiglio Nazionale delle Ricerche (CNR),
Via Amendola 122/D, 70126 Bari, Italy*

(Dated: May 10, 2024)

Abstract

The conformational and dynamical properties of active ring polymers are studied by numerical simulations. The two-dimensionally confined polymer is modeled as a closed bead-spring chain, driven by tangential forces, put in contact with a heat bath described by the Brownian multiparticle collision dynamics. Both phantom polymers and chains comprising excluded volume interactions are considered for different bending rigidities. The size and shape are found to be dependent on persistence length, driving force, and bead mutual exclusion. The lack of excluded volume interactions is responsible for a shrinkage of active rings when increasing driving force in the flexible limit while the presence induces a moderate swelling of chains. Internal dynamics of flexible phantom active rings shows activity-enhanced diffusive behavior at large activity values while, in the case of self-avoiding active chains, it is characterized by active ballistic motion not depending on stiffness. The long-time dynamics of active rings is marked by rotational motion whose period scales as the inverse of the applied tangential force, irrespective of persistence length and beads self-exclusion.

* antonio.lamura@cnr.it

I. INTRODUCTION

Last twenty years registered a growing interest towards active matter [1–4]. This is made of out-of-equilibrium interacting units capable of absorbing energy from their environment and transforming it into motion. An interesting example is provided by active polymer-like structures where the presence of active noise and/or internal propulsion, interacting with deformability, is responsible for intriguing new phenomena, investigated both theoretically and numerically [5–18]. Nature provides numerous realizations showing how activity is crucial in determining both structural and dynamical properties. Among others, actin filaments and microtubules are prototypes of filamentous structures, subject to local active forces exerted by biomolecular motors, capable of performing different activities at the biological level [19, 20]. For example, microtubules placed on kinesin motility assays can undergo active self-organization to obtain more ordered structures such as bundles [21] and rings [22]. Such closed structures are very common and can be observed in chromosomes inside bacteria [23], in DNA and RNA arranging in loops [24, 25], in actomyosin rings [26], and in microtubules on dynein-coated surfaces [27] whose dynamics is greatly affected by the circular form [28].

Very recently some studies have investigated structures and dynamic behaviors of active rings. In three spatial dimensions active Brownian [29] and tangentially driven [30, 31] ring polymer models have been considered. In the former case it is found that the action of local active random forces enhances conformal fluctuations [29] while in the latter one, the local tangent force causes small rings to swell and large rings to collapse with an arrested dynamics in the case of flexible rings [30]. Neglecting excluded volume interactions allows an analytical study of the dynamics of semiflexible active polar ring polymers [31] which reveals that conformations are independent on activity and characterized by a rotational motion. This resembles the tank-treading motion observed for passive rings [32–35] and vesicles [36, 37] when subject to an external shear flow. The interplay of local polar and long-range activities on the swelling and collapse of flexible ring polymers has been also considered [38].

In the two-dimensional case very few studies addressed the behavior of active ring polymers. Active Brownian models have been adopted to mimic mammalian cells [39] and to investigate the motion of active rings in porous media [40]. Despite of this, the problem is interesting since several experiments showed that it is possible to assemble microtubules, on a

motor protein-fixed surface [22, 28, 41], in ring shapes which are characterized by rotational motion [27]. Due to the peculiar dynamic behavior, it appears very engaging to understand such patterns which strongly depend on the topological constraints in two dimensions. This is precisely the aim of the present study where the effects of excluded volume interactions are explicitly considered in the case of active polymer rings.

We introduce a discrete model of a closed semiflexible polymer whose beads are subject to a force tangentially oriented with respect to the polymer backbone. Excluded volume interactions are taken into account in order to highlight their roles in the observed dynamics since these forces are known to be relevant in the case of two-dimensional passive rings in the limit of small bending rigidity [42, 43]. Hydrodynamic interactions are ignored due to the strong interaction between rings and substrates in two dimensions thus allowing the use of the free-draining approximation. For this reason the polymer is placed in contact with a Brownian heat bath and its dynamics is numerically studied by using the Brownian version [44] of the multiparticle collision dynamics [45, 46]. We find that the size and shape, measured by the radius of gyration and by the asphericity, respectively, depend on persistence length, excluded volume interactions, and active force. In the limit of flexible rings, phantom chains decrease in size when increasing activity while rings with conserved topology present a moderate swelling, becoming more roundish in both cases. In the opposite limit of stiff rings, excluded volume interactions are not crucial in determining conformations which are independent on activity. Flexible phantom active rings show enhanced diffusive dynamics while self-avoiding active chains display ballistic dynamic behavior not depending on stiffness. The long-time dynamics is characterized by a reptation motion for all bending rigidities which, in the case of stiff rings, resembles the tank-treading motion observed for two-dimensional sheared vesicles [47–49]. The rotational period is found to scale as the inverse of the active force.

The numerical model for the polymer and the Brownian heat bath is introduced in Sec. II. The results for the conformations and the dynamics are reported in Sec. III. Finally, Sec. IV is devoted to discuss the main findings presenting some conclusions.

II. MODEL AND METHOD

A closed chain of length L is considered in two spatial dimensions. It is composed of N beads, each having mass M , whose internal interactions are due to different contributions. Consecutive beads interact via the harmonic potential

$$U_{bond} = \frac{\kappa_h}{2} \sum_{i=1}^N (|\mathbf{r}_{i+1} - \mathbf{r}_i| - l)^2, \quad (1)$$

where κ_h is the spring constant, \mathbf{r}_i indicates the position vector of the i -th bead ($i = 1, \dots, N$) with $\mathbf{r}_{N+1} = \mathbf{r}_1$ and $\mathbf{r}_0 = \mathbf{r}_N$, and l is the average bond length. A bending potential is considered to enforce chain stiffness and is given by

$$U_{bend} = \kappa \sum_{i=1}^N (1 - \cos \theta_i) \quad (2)$$

where κ controls the bending rigidity and θ_i is the angle between two consecutive bond vectors. In the following, chain stiffness is characterized in terms of the length $L_p = 2\kappa l/k_B T$ which corresponds to the polymer persistence length in the worm-like chain limit [50]. Here $k_B T$ is the thermal energy, T is the temperature, and k_B is Boltzmann's constant. Excluded volume interactions between non-bonded beads are modeled by the truncated and shifted Lennard-Jones potential

$$U_{ex} = 4\epsilon \left[\left(\frac{\sigma}{r} \right)^{12} - \left(\frac{\sigma}{r} \right)^6 + \frac{1}{4} \right] \Theta(2^{1/6} \sigma - r), \quad (3)$$

where ϵ is the volume-exclusion energy, r is the distance between two non-connected beads, and $\Theta(x)$ is the Heaviside function ($\Theta(x) = 0$ for $x < 0$ and $\Theta(x) = 1$ for $x \geq 0$). This potential avoids chain self-crossings so to preserve the ring topology.

Finally, an active force \mathbf{F}_i^a ($i = 1, \dots, N$) is applied tangentially to the filament at the position of each bead. In the present paper we adopt a push-pull type force [6, 8, 13, 31]. By assuming that molecular motors are homogeneously distributed along a bond, it is reasonable to consider that each bond is subject to a constant force, along its direction, given by $f^a(\mathbf{r}_i - \mathbf{r}_{i-1})/l$ ($i = 1, \dots, N$) [6]. This force has magnitude f^a since the bond length $|\mathbf{r}_i - \mathbf{r}_{i-1}|$ is constrained to be l by using a very high value of the spring constant κ_h in (1). The force on each bond is then equally distributed between the adjacent beads so that, say, on the bead i there is a contribution $f^a(\mathbf{r}_i - \mathbf{r}_{i-1})/(2l)$ along the inward bond and a contribution

$f^a(\mathbf{r}_{i+1} - \mathbf{r}_i)/(2l)$ along the outward bond. The total net force acting on the i -th bead is the sum of these two terms

$$\mathbf{F}_i^a = \frac{f^a}{2l} (\mathbf{r}_{i+1} - \mathbf{r}_{i-1}), i = 1, \dots, N. \quad (4)$$

The expression (4) is such that the sum of active forces along the discrete ring, $\sum_{i=1}^N \mathbf{F}_i^a$, is zero [31]. Moreover, the value of the force (4) depends on the relative positions of the beads $i - 1$ and $i + 1$, varying between 0, when the two consecutive bonds are antiparallel, and f^a , when the bonds are parallel. In other studies a constant tangent force, acting on all the beads, has been considered [30, 51, 52]. The strength of the total active force is quantified by the Péclet number $Pe = f^a NL/(k_B T)$ [8, 31]. An alternative definition of the Péclet number, $Pe^* = f^a l/(k_B T) = Pe/N^2$, being $L = Nl$, is sometimes used in the literature [30]. Newton's equations of motion of beads are integrated by the velocity-Verlet algorithm with time step Δt_p [53, 54].

The ring is kept in contact with a Brownian heat bath which is modeled by making use of the Brownian multiparticle collision (MPC) method [44, 46, 55] where hydrodynamics is ignored. Every bead interacts with ρ virtual solvent particles of mass m in order to simulate the interaction with a fluid volume. Since it is not necessary to keep track of the positions of the solvent particles in the present algorithm [44], it is sufficient to couple each bead with an effective virtual solvent particle with momentum sampled from a Maxwell-Boltzmann distribution of variance $\rho m k_B T$ and zero mean. The interaction process proceeds via the stochastic rotation dynamics of the MPC method [46, 56, 57]. The relative velocity of each polymer bead, with respect to the center-of-mass velocity of the bead and its corresponding virtual solvent particle, is randomly rotated by angles $\pm\alpha$. Collisions are then executed at time intervals Δt , with $\Delta t > \Delta t_p$. It has been shown that the evolution equation of the MPC model for the solute particle takes the form of a discretized Langevin equation for which the expression of the friction coefficient has been obtained [55].

Simulations are carried out with the choices $\alpha = 130^\circ$, $\Delta t = 0.1t_u$, with time unit $t_u = \sqrt{ml^2/(k_B T)}$, $M = \rho m$ with $\rho = 5$, $\kappa_h l^2/(k_B T) = 10^4$, $\sigma/l = 1$, $N = L/l = 50$, and $\Delta t_p = 10^{-2}\Delta t$. In some cases, longer rings with $N = 100, 200$ beads have been also considered. A larger value of the ratio σ/l , which might be experimentally relevant, would cause the overlap of neighboring beads with a smoothing of the interaction potential and, eventually, only minor quantitative changes in the following results. The value of κ_h is such

to ensure that bond length fluctuations are negligible in any non-equilibrium condition.

III. NUMERICAL RESULTS

We consider rings with persistence lengths ranging from the flexible limit ($L_p/L = 0$) to the stiff one ($L_p/L = 40$). The active force f^a is varied to access a wide interval of Péclet number ($0 \leq Pe \leq 5 \times 10^4$ - $0 \leq Pe^* \leq 20$). Finally, in order to incorporate excluded volume effects, the value $\epsilon = k_B T$ is used referring to the model as a self-avoiding active ring (SAR). To point up topological effects, a comparison with self-crossing rings is also carried out by setting $\epsilon = 0$. In this latter case we refer to the model as a phantom active ring (PAR). For the considered set of parameters, the friction coefficient ξ [55] acting on each bead is such that $M/\xi \lesssim 2.0 \times 10^{-6}\tau_r, 8.5 \times 10^{-5}\tau_r$ for self-avoiding and phantom rings, respectively. This ensures that the dynamics is close to the overdamped one so that inertial effects are negligible for the results in the following. Here and in the rest of the paper, τ_r denotes the polymer relaxation time in the passive case and is determined by considering the time decay of the ring-diameter autocorrelation function (see details when discussing Fig. 10). It results to be $\tau_r \simeq 6.5 \times 10^4 t_u, 1.5 \times 10^3 t_u$ for self-avoiding and phantom flexible rings, respectively, and $\tau_r \simeq 1.6 \times 10^5 t_u$ when $L_p/L = 40$ where there are no differences between the two models. Polymers are initialized in a circular shape and equilibrated up to time $10^6 t_u$, much longer than any polymer relaxation time. Then, data are collected in single runs for every parameter set over time intervals of duration $\simeq 50\tau_r$, and averaged. In the case of the PAR model with $L_p/L = 0.4$ at $Pe = 2.5 \times 10^4$, averages are obtained from three different realizations, each of duration up to $150\tau_r$.

A. Polymer conformations

By varying activity and stiffness, rings can attain different configurations. In order to characterize the observed patterns, the gyration tensor

$$G_{\alpha\beta} = \frac{1}{N} \sum_{i=1}^N \Delta r_{i,\alpha} \Delta r_{i,\beta} \quad (5)$$

is computed. Here $\Delta r_{i,\alpha}$ is the position of the i -th bead in the center-of-mass reference frame of the polymer and the Greek index indicates the Cartesian component. The two eigenvalues

λ_1 and λ_2 , with $\lambda_1 > \lambda_2$, of the tensor (5) are extracted to calculate the gyration radius

$$R_g^2 = \lambda_1 + \lambda_2 \quad (6)$$

which measures the total size of the ring. The asphericity

$$A = \frac{(\lambda_1 - \lambda_2)^2}{(\lambda_1 + \lambda_2)^2} \quad (7)$$

is also computed to provide information about the shape, being $0 \leq A \leq 1$ with $A = 0$ for a circle and $A = 1$ for a rod.

The computed values of $\langle R_g^2 \rangle^{1/2}$, normalized to the radius of gyration $R_c = L/(2\pi)$ of a rigid circle, are depicted versus the Péclet number in Fig. 1 for different values of the persistence length L_p in the case of SAR and PAR models. The left panel shows data in the flexible regime corresponding to chains for which the values of the gyration radius in the passive limit, $Pe \rightarrow 0$, are different for self-avoiding (filled symbols) and phantom (empty symbols) rings [43]. The difference in the radii is due to the conserved circular topology in the SAR model thanks to self-avoiding effects. In this model polymers show larger sizes with respect to the PAR model. On the contrary, the bonds of phantom rings overlap to maximize the configurational entropy because of flexibility [43] thus producing more compact structures. Radii increase with the persistence length in both models while the relative differences reduce. Activity does not produce any significant change in the radius of gyration up to $Pe \simeq 10^3$. For values $Pe \gtrsim 10^4$, the behavior varies with the considered model and the conformations depend on activity. Some typical configurations are reported in the bottom part of Fig. 1. This latter range of activity is experimentally relevant: For example, in the case of microtubules of length $L = 1\mu m$ with $N = 10$ active motors, each with force $f^a = 6pN$, it would be $Pe \simeq 10^4$ at room temperature [31, 58]. Phantom rings tend to shrink while self-avoiding rings swell. In the case of fully flexible chains ($L_p/L = 0$) when $Pe = 5 \times 10^4$, the root mean-square radius of gyration reduces by approximately 25% for PAR model and increases by approximately 15% for SAR model with respect to the values at equilibrium. We note here that the shrinkage of phantom chains in two dimensions is larger compared to the value ($\simeq 10\%$) found in three dimensions [31] using a similar discrete model for the same Péclet number, thus pointing out the relevance of space dimensionality on conformations. The probability distribution functions $P(R_g/R_c)$ of the radius of gyration are shown for PAR and SAR models with $L_p/L = 0$ in the panels (a) and (c), respectively, of

Fig. 2 for different values of activity. In both models, the mode of the distribution increases with Pe and the width becomes narrower suggesting that fluctuations are suppressed by activity (see Movie 1 given in the supplementary material). By increasing the stiffness, the variations of $\langle R_g^2 \rangle^{1/2}$ with respect to the equilibrium value reduce and become negligible in the case of self-avoiding rings for which a very small contraction ($\simeq 3\%$) can be appreciated when $L_p/L = 0.2$. At value of bending rigidity such that $L_p/L \simeq 0.4$, the stiff regime is entered. In the passive limit $Pe \rightarrow 0$, the values of the gyration radius appear indistinguishable at fixed bending rigidity, irrespective of excluded volume interactions, as a consequence of the mechanical constraints exerted by stiffness (see Fig. 1 (b)). The global size of rings increases with stiffness to become comparable to that of a rigid ring for very stiff chains ($L_p/L = 40$). When active polymers are considered, they show negligible variations in size except in the case of phantom active rings with $L_p/L = 0.4$. In this latter case, the gyration radius displays a non-monotonic dependence on the Péclet number due to different conformations which can be assumed by the ring. This is reflected in the probability distribution function of R_g , shown in Fig. 2 (b), that becomes multimodal in the cases with $Pe = 2.5 \times 10^4, 5 \times 10^4$. Without the topology constraint enforced by excluded volume interactions, activity is able to deform the chain despite its bending rigidity. The interplay with fluctuations produces different configurations of variable duration, observable during very long time dynamics. Typical patterns, corresponding to the three peaks of $P(R_g/R_c)$ with $Pe = 2.5 \times 10^4$, are illustrated in Fig. 3. In the case of self-avoiding active rings with $L_p/L = 0.4$, activity does not change the global size. However, distribution functions become skewed (see Fig. 2 (d)) since rings continuously shrink and swell during their dynamics (see Movie 2 given in the supplementary material). This effect reduces when increasing the bending rigidity so that rings behave as rigid circles. Indeed, when $L_p/L \gtrsim 1$, no appreciable difference can be observed in the behavior between PAR and SAR models since self-exclusion becomes irrelevant. This is due to the fact that bonds are separated from each other because of the high bending rigidity of stiff polymers. More details about the dynamics will be provided in the following Section.

In order to gain further insight into the observed patterns of active rings, the equal time bond correlation function is computed. It is defined as

$$\langle \cos \theta(s) \rangle = \frac{\langle \mathbf{t}_{i+s} \cdot \mathbf{t}_i \rangle}{l^2} \quad (8)$$

where $\mathbf{t}_i = \mathbf{r}_{i+1} - \mathbf{r}_i$ is the bond vector and s is the contour separation. The closed topology guarantees the property $\langle \cos \theta(s) \rangle = \langle \cos \theta(N - s) \rangle$. Figure 4 depicts the bond correlation function for the persistence lengths $L_p/L = 0, 0.4$ with $Pe = 2.5 \times 10^4$. Flexible phantom rings show a very fast decay at small separations followed by anti-correlation on a distance of about two bonds before reaching complete decorrelation at a contour separation of about 6 bonds. This suggests the presence of small wraps of few beads that favor the contraction in size. In contrast, flexible self-avoiding active rings manifest a larger directional correlation on short distance due to excluded volume effects that restrict the possible conformations. Owing to the preserved circular topology, the correlation function becomes negative on separations $s/N \simeq 1/2$. As already observed, stiffness is responsible of increasing the size of rings. In the case of self-avoiding active rings with $L_p/L = 0.4$, this produces a larger correlation between bonds which are strongly anti-correlated on distances $s/N \simeq 1/2$ as in the case of rigid passive rings [42]. When considering semiflexible phantom active rings, the presence of the structure with two interlaced rings, shown in Fig. 3 (c), determines bond anti-correlation at separations $s/N \simeq 1/4$ and small correlation at $s/N \simeq 1/2$.

In order to better evaluate the effect of activity on the shape of active rings, the average asphericity is plotted in Fig. 5 for the flexible (panel (a)) and stiff (panel (b)) regimes. In the former case, asphericity presents a non-monotonic dependence on stiffness when $Pe \rightarrow 0$, as observed in Ref. [43], with self-exclusion warranting more circular shapes. The effect of activity is to make rings more roundish in both models with the exception of the PAR model with $L_p/L = 0.2$ when activity favors elongated structures with respect to the passive limit. As far as the bending rigidity is negligible, our results give $\langle A \rangle \simeq 0.26$ in the passive case, as predicted in the Gaussian limit [59]. The observed small wraps at high activity favor local back folding so that rings are able to gain even more compact conformations (see Fig. 1 (a)), while reducing their asphericity with respect to the passive case. Once bending rigidity comes into play (at values $L_p/L \simeq 0.2$), phantom active rings can still reduce the gyration radius due to self-crossing while assuming a more eccentric elliptical shape. The corresponding probability distributions $P(A)$ are highly skewed with a maximum at $A = 0$ and long tails, as it can be seen in Fig. 6 (a,c) for flexible rings ($L_p/L = 0$). The effect of activity is to increase the height of the maximum of distributions while slightly shortening tails. For stiff active rings (Fig. 5 (b)) it is possible to observe that activity induces slightly more elongated shapes with respect to the passive case though this effect reduces when increasing stiffness.

Only for phantom active rings with $L_p/L = 0.4$, a non-monotonic dependence on activity is visible due to the observed conformations (see Fig. 3) and the peculiar dynamics, as previously discussed. This is also reflected in the probability distributions shown Fig. 6 (b) for $L_p/L = 0.4$. The distribution $P(A)$ is characterized by a linear decay as far as $Pe \lesssim 10^4$. For larger values of activity longer tails and pronounced shoulders appear in the distribution $P(A)$. In the case of self-avoiding active rings (Fig. 6 (d)), the role played by activity is to produce slightly longer tails while poorly affecting the behavior at small values of A .

B. Dynamical behavior

In this Section we describe and characterize the dynamical behavior of active rings once the steady state has been reached. When $Pe \lesssim 1$, there are no effects induced by the applied tangential force and rings behave as in the passive case with diffusive translational motion of the center of mass (see the following discussion). By increasing activity, rings are set in a slow rotational motion due to the applied force though this rotation is not continuous in time. In order to illustrate and quantify the described behavior, it is useful to consider the ring diameter, defined as $\mathbf{R}_d = \mathbf{r}_{N/2+1} - \mathbf{r}_1$. The time dependence of the x -component R_{dx} is reported in Fig. 7 in the case of a flexible self-avoiding ring at different values of activity. Once $Pe \sim o(10^2)$, a steady rotation of active rings can be observed. During steady rotation, the vector \mathbf{R}_d rotates continuously so that its components oscillate periodically in time. This behavior can be used to infer the characteristic rotation frequency ω . This is determined by a spectral analysis (see the inset of Fig. 7 (d)) of the time series $R_{dx}(t)$. The computed periods of rotation, $T = 2\pi/\omega$, are shown in Fig. 8 for different persistence lengths and rings of lengths $L = 50l, 100l, 200l$. It is evident that the period T follows a power-law decay with dependence $(Pe/L^3)^{-1}$, irrespective of the bending rigidity and ring average size at high activity. Our results confirm what analytically predicted for three-dimensional phantom active rings that undergo active tank-treading motion with frequency $\omega = (Pe/L^3)(2\pi lk_B T/\xi) = f^a/(R_c \xi)$ which is proportional to the tangential velocity f^a/ξ and independent of the effective ring size. [31]. Moreover, here we find evidence that the period is not depending on excluded volume interactions in two dimensions. In the case of the phantom flexible chain, a compact conformation is observed at $Pe \simeq 10^2$ and thermal noise deeply influences ring rotation so that the observed spectrum of frequencies is quite

broad. Phantom active rings require larger values of activity or of stiffness with respect to self-excluding active rings in order to establish a uniform rotational motion.

Sizes and shapes of active rings in the steady state show a poor dependence on the applied force as far as $Pe \lesssim 10^4$, as already discussed in the previous Section. However, when entering the regime of experimentally relevant Péclet numbers, rings undergo large morphological deviations with respect to equilibrium. Phantom active rings, despite the initial circular configuration, can be driven, going through intermediate structures (see panel (b) of Fig. 3), into more compact configurations (see panel (c) of Fig. 3). Simulations for the PAR model have been conducted at $Pe = 2.5 \times 10^4$ for different values of the persistence length. It appears that when $0.3 \lesssim L_p/L \lesssim 0.45$, rings spontaneously assume the double ring conformation with $R_g/R_c \simeq 0.52$ (corresponding to the typical value of R_g for the conformation of Fig. 3 (c)). This latter structure can spontaneously disentangle with a lifetime which is longer at $L_p/L \simeq 0.4$. This behavior can be observed in the time dependence of the gyration radius and of the asphericity in Fig. 9 for the PAR model with $L_p/L = 0.4$ at $Pe = 2.5 \times 10^4$ on a very long time run of duration $150\tau_r \simeq 7 \times 10^4 T$. Starting from the initial circular shape, phantom rings can self-cross assuming conformations similar to the one of Fig. 3 (b) with an elongated shape resembling the number eight. This is possible only in a narrow range centered at $L_p/L \simeq 0.4$ since the “eight configuration” is compatible with this value of the persistence length. Due to thermal fluctuations, it can happen that one of the two sub-rings moves towards the other one trespassing the mutual crossing point to give the double ring conformation. Despite this costs a strong local bending, the double ring is always observed at $L_p/L = 0.4$ in all the considered runs at very high Péclet number. In the case of active rings comprising excluded volume interactions, activity is responsible of inducing temporary elongated configurations as illustrated in Fig. 9 by the peaks of asphericity corresponding to the reduction of the radius of gyration (see also Movie 2 in the supplementary material).

In order to further characterize the rotational behavior, it is useful to consider the normalized time-correlation function of the ring diameter $\langle \mathbf{R}_d(t) \cdot \mathbf{R}_d(0) \rangle / \langle \mathbf{R}_d^2(0) \rangle$. In the left panel of Fig. 10 the normalized autocorrelation function is plotted for a flexible self-avoiding ring for different values of activity. In the passive case, the function exhibits an exponential decay, $\exp(-t/\tau_r)$, which is used to determine the polymer relaxation time τ_r . When $Pe = 10$ no relevant difference can be appreciated with respect to equilibrium on time scales

comparable to the relaxation time. The increase of activity is responsible for producing an oscillatory behavior which is modulated in time by the same decay of the passive ring. The damped oscillatory pattern with a shorter period is maintained when the Péclet is further increased. The comparison in the behavior of the autocorrelation function of the ring diameter between the PAR and SAR models is reported in the panel (b) of Fig. 10 for different bending rigidities with $Pe = 10^3$. In the case of flexible phantom active rings, the correlation function shows an exponential decay since the observed compact structure, due to the lack of any bending rigidity, requires larger values of activity to observe oscillations. On the contrary, self-avoiding active rings present the damped oscillatory behavior thanks to excluded volume effects that preserve the circular topology avoiding any collapse of the chain while rotating. Oscillations are clearly observable in the correlation functions of semiflexible, both phantom and self-excluding, active rings. The amplitudes are larger in the latter case due to the longer relaxation times and increase with bending rigidity to become indistinguishable between the two models in the limit of stiff rings. As far as oscillations are well defined, the numerical data of the autocorrelation function are very well approximated (see Fig. 10 (b)) by the theoretical prediction [31]

$$\frac{\langle \mathbf{R}_d(t) \cdot \mathbf{R}_d(0) \rangle}{\langle \mathbf{R}_d^2(0) \rangle} \approx \cos(2\pi t/T) \exp(-t/\tau_r), \quad (9)$$

where the values of T and τ_r , computed in the present simulations, are used.

Finally, the beads mean-square displacement (MSD) $\langle (\mathbf{r}_i(t) - \mathbf{r}_i(0))^2 \rangle$ is computed which allows the characterization of the translational motion of ring. Due to the ring topology, the beads MSD is independent of the point location and receives a contribution from the center-of-mass motion, $\langle \Delta \mathbf{r}_{cm}^2(t) \rangle$, and another one from the internal dynamics, $\langle \Delta \mathbf{r}^2(t) \rangle$, so that one can write $\langle (\mathbf{r}_i(t) - \mathbf{r}_i(0))^2 \rangle = \langle \Delta \mathbf{r}_{cm}^2(t) \rangle + \langle \Delta \mathbf{r}^2(t) \rangle$. Since the sum of all internal and active forces over the whole ring vanish, the center-of-mass motion is purely diffusive depending only on thermal fluctuations and not on activity. In this way the quantity $\langle \Delta \mathbf{r}^2(t) \rangle$, which is related the beads MSD relative to the center-of-mass MSD, provides information on the ring internal dynamics. The MSD $\langle \Delta \mathbf{r}^2(t) \rangle$ for self-avoiding flexible ($L_p/L = 0$) and stiff active rings ($L_p/L = 40$) with different activities are reported in Fig. 11. In the case without any stiffness (panel (a)) the sub-diffusive exponent 0.6 is found in the time range $t \ll \tau_r$ when thermal effects prevail on active contributions, as predicted by the Rouse model of two-dimensional flexible polymers with excluded volume interactions [60]. For large Péclet

numbers, $Pe \gtrsim 10^4$, an active ballistic time regime is observed with $\langle \Delta \mathbf{r}^2(t) \rangle \sim t^2$. For longer times, oscillations, due to the active tank-treading, appear in the MSD which then goes to a plateau when $t \gtrsim \tau_r$. This behavior, due to the mutual repulsion among beads, is different from what is found when considering flexible phantom rings. In this case the sub-diffusive behavior $t^{1/2}$ holds when $t \ll \tau_r$. The MSD shows the activity-enhanced linear time regime at high values of activity ($Pe \simeq 10^4$) followed by oscillations at longer times, as predicted in three dimensions [31]. The MSD of stiff polymers (panel (b)) exhibits an initial time dependence $t^{0.7}$. The exponent 0.7 slightly underestimates the predicted value 3/4 [61] due to the finite ring length [60]. A linear time dependence [62] is then observed at late times when $Pe \lesssim 1$. Strong activity induces the active ballistic time regime followed in time by oscillations. In this case we find that the numerical values of $\langle \Delta \mathbf{r}^2(t) \rangle$ are very well described (see Fig. 11 (b)) by the theoretical prediction [31]

$$\langle \Delta \mathbf{r}^2(t) \rangle / L^2 \approx \left[1 - \cos(2\pi t/T) e^{-t/\tau_r} \right] / (2\pi^2), \quad (10)$$

where the computed values of T and τ_r are used.

IV. DISCUSSION AND CONCLUSIONS

The conformations and dynamics of tangentially-driven active ring polymers have been numerically studied. The discrete closed chain has been confined in two dimensions and coupled to a Brownian heat bath performed by the stochastic implementation of the multi-particle collision dynamics. Both phantom and self-avoiding rings have been considered for different bending rigidities ranging from the flexible to the stiff limit.

Excluded volume interactions affect the conformations of flexible active rings: Polymers with self-excluding beads swell up to 15% while phantom chains shrink down to 25% at high values of the Péclet number, in both cases attaining more circular shapes. No appreciable difference is observed between the two models of active rings in the semiflexible limit with the exception of phantom rings with persistence length slightly less than half of the total chain length. In this latter case activity can induce more compact conformations since the initial circular topology is not conserved. The observed double ring conformation would be permitted in the presence of excluded-volume interactions in three spatial dimensions, or quasi two-dimensional confinement, so that activity might trigger the transition to this

conformation in real systems, eventually detectable in experimental setups. The mean-square displacement relative to the center-of-mass MSD allows us to capture the internal dynamics. At intermediate time scales, flexible phantom active rings shows an activity-enhanced diffusive regime at large activity values. This is different from what observed in the case of self-avoiding active chains for which internal motion is ballistic, independently on stiffness. At high values of activity, rings exhibit active tank-treading motion whose period scales as the inverse of the applied tangential force, irrespective of both persistence length and beads self-exclusion.

Excluded volume interactions have been shown to play a major role in capturing the phenomenology of two-dimensional flexible active rings thus it appears very interesting to extend the present study to melts where both inter- and intra-bead mutual repulsions will be relevant. Moreover, the action of an external shear flow would possibly enrich the described picture impacting on the observed conformations and dynamics, as observed for active Brownian linear polymers [63, 64]. This would require to separate out effects of internal and external stresses, as far as timescales are not separable, in order to obtain a complete description of the system.

ACKNOWLEDGMENTS

Funding from MIUR Project No. PRIN 2020/PFCXPE is acknowledged. This work was performed under the auspices of GNFM-INdAM.

Appendix: Movies Description

In this Section we provide a brief description of the movies accompanying the paper.

- **Movie 1: Flexible self-avoiding active ring**

The movie illustrates the motion of a flexible self-avoiding active ring with $L_p/L = 0$ for $Pe = 2.5 \times 10^4$ in the center-of-mass reference frame. Frames are taken at time intervals $\Delta t/T \simeq 0.11$ where T is the computed rotational period. To illustrate the clockwise rotation, the beads 1 and $N/2 + 1$ are colored blue and yellow, respectively.

- **Movie 2: Semiflexible self-avoiding active ring**

The movie illustrates the motion of a semiflexible self-avoiding active ring with $L_p/L =$

0.4 for $Pe = 2.5 \times 10^4$ in the center-of-mass reference frame. Frames are taken at time intervals $\Delta t/T \simeq 0.11$ where T is the computed rotational period. To illustrate the clockwise rotation, the beads 1 and $N/2 + 1$ are colored blue and yellow, respectively.

-
- [1] M. C. Marchetti, J. F. Joanny, S. Ramaswamy, T. B. Liverpool, J. Prost, M. Rao, and R. A. Simha, Hydrodynamics of soft active matter, *Rev. Mod. Phys.* **85**, 1143 (2013).
 - [2] J. Elgeti, R. G. Winkler, and G. Gompper, Physics of microswimmers—single particle motion and collective behavior: a review, *Rep. Prog. Phys.* **78**, 056601 (2015).
 - [3] C. Bechinger, R. D. Leonardo, H. Löwen, C. Reichhardt, G. Volpe, and G. Volpe, Active particles in complex and crowded environments, *Rev. Mod. Phys.* **88**, 045006 (2016).
 - [4] R. G. Winkler, J. Elgeti, and G. Gompper, Active polymers—emergent conformational and dynamical properties: A brief review, *J. Phys. Soc. Jpn.* **86**, 101014 (2017).
 - [5] J. Elgeti and G. Gompper, Self-propelled rods near surfaces, *EPL* **85**, 38002 (2009).
 - [6] H. Jiang and Z. Hou, Motion transition of active filaments: rotation without hydrodynamic interactions, *Soft Matter* **10**, 1012 (2014).
 - [7] A. Ghosh and N. S. Gov, Dynamics of active semiflexible polymers, *Biophys. J.* **107**, 1065 (2014).
 - [8] R. E. Isele-Holder, J. Elgeti, and G. Gompper, Self-propelled worm-like filaments: spontaneous spiral formation, structure, and dynamics, *Soft Matter* **11**, 7181 (2015).
 - [9] R. E. Isele-Holder, J. Jäger, G. Saggiorato, J. Elgeti, and G. Gompper, Dynamics of self-propelled filaments pushing a load, *Soft Matter* **12**, 8495 (2016).
 - [10] T. Eisenstecken, G. Gompper, and R. G. Winkler, Internal dynamics of semiflexible polymers with active noise, *J. Chem. Phys.* **146**, 154903 (2017).
 - [11] K. R. Prathyusha, S. Henkes, and R. Sknepnek, Dynamically generated patterns in dense suspensions of active filaments, *Phys. Rev. E* **97**, 022606 (2018).
 - [12] O. Duman, R. E. Isele-Holder, J. Elgeti, and G. Gompper, Collective dynamics of self-propelled semiflexible filaments, *Soft Matter* **14**, 4483 (2018).
 - [13] S. K. Anand and S. P. Singh, Structure and dynamics of a self-propelled semiflexible filament, *Phys. Rev. E* **98**, 042501 (2018).

- [14] M. Foglino, E. Locatelli, C. A. Brackley, D. Michieletto, C. N. Likos, and D. Marenduzzo, Non-equilibrium effects of molecular motors on polymers, *Soft Matter* **15**, 5995 (2019).
- [15] R. G. Winkler and G. Gompper, The physics of active polymers and filaments, *J. Chem. Phys.* **153**, 040901 (2020).
- [16] T. Eisenstecken and R. G. Winkler, Path integral description of semiflexible active Brownian polymers, *J. Chem. Phys.* **156**, 064105 (2022).
- [17] C. A. Philipps, G. Gompper, and R. G. Winkler, Tangentially driven active polar linear polymers - an analytical study, *J. Chem. Phys.* **157**, 194904 (2022).
- [18] M. Vatin, S. Kundu, and E. Locatelli, Conformation and dynamics of partially active linear polymers, *Soft Matter* **20**, 1892 (2024).
- [19] N. Hirokawa, Kinesin and dynein superfamily proteins and the mechanism of organelle transport, *Science* **279**, 519 (1998).
- [20] M. Bachand, A. Trent, B. Bunker, and G. Bachand, Physical factors affecting kinesin-based transport of synthetic nanoparticle cargo, *J. Nanosci. Nanotechnol.* **5**, 718 (2005).
- [21] R. Kawamura, A. Kakugo, Y. Osada, and J. Gong, Selective formation of a linear-shaped bundle of microtubules, *Langmuir* **26**, 533 (2010).
- [22] R. Kawamura, A. Kakugo, K. Shikinaka, Y. Osada, and J. P. Gong, Ring-shaped assembly of microtubules shows preferential counterclockwise motion, *Biomacromolecules* **9**, 2277 (2008).
- [23] F. Wu, A. Japaridze, X. Zheng, J. Wiktor, J. W. J. Kerssemakers, and C. Dekker, Direct imaging of the circular chromosome in a live bacterium, *Nat. Commun.* **10**, 2194 (2019).
- [24] R. Schaleif, Dna looping, *Annu. Rev. Biochem.* **61**, 192 (1992).
- [25] T. S. Alexiou, P. V. Alatas, D. G. Tsalikis, and V. G. Mavrantzas, Conformational and dynamic properties of short dna minicircles in aqueous solution from atomistic molecular dynamics simulations, *Macromolecules* **53**, 5903 (2020).
- [26] S. P. Pearce, M. Heil, O. E. Jensen, G. W. Jones, and A. Prokop, Curvature-sensitive kinesin binding can explain microtubule ring formation and reveals chaotic dynamics in a mathematical model, *Bulletin of Mathematical Biology* **80**, 3002 (2018).
- [27] M. Ito, A. M. R. Kabir, D. Inoue, T. Torisawa, Y. Toyoshima, K. Sada, and A. Kakugo, Formation of ring-shaped microtubule assemblies through active self-organization on dynein, *Polym. J.* **46**, 220 (2014).
- [28] J. J. Keya, A. M. R. Kabir, and A. Kakugo, Synchronous operation of biomolecular engines,

- Biophys. Rev. **12**, 401 (2020).
- [29] S. M. Mousavi, G. Gompper, and R. G. Winkler, Active Brownian ring polymers, *J. Chem. Phys.* **150**, 064913 (2019).
- [30] E. Locatelli, V. Bianco, and P. Maggaretti, Active polymer rings: activity-induced collapse and dynamic arrest, *Phys. Rev. Lett.* **126**, 097801 (2021).
- [31] C. A. Philipps, G. Gompper, and R. G. Winkler, Dynamics of active polar ring polymers, *Phys. Rev. E* **105**, L062591 (2022).
- [32] W. Chen, J. Chen, and L. An, Tumbling and tank-treading dynamics of individual ring polymers in shear flow, *Soft Matter* **9**, 4312 (2013).
- [33] P. S. Lang, B. Obermayer, and E. Frey, Dynamics of a semiflexible polymer or polymer ring in shear flow, *Phys. Rev. E* **89**, 022606 (2014).
- [34] M. Liebetreu, M. Ripoll, and C. N. Likos, Trefoil knot hydrodynamic delocalization on sheared ring polymers, *ACS Macro Lett.* **7**, 447 (2018).
- [35] M. Liebetreu and C. N. Likos, Hydrodynamic inflation of ring polymers under shear, *Communications Materials* **1**, 4 (2020).
- [36] H. Noguchi and G. Gompper, Fluid vesicles with viscous membranes in shear flow, *Phys. Rev. Lett.* **93**, 258102 (2004).
- [37] J. Beaucourt, F. Rioual, T. Seon, T. Biben, and C. Misbah, Steady to unsteady dynamics of a vesicle in a flow, *Phys. Rev. E* **69**, 011906 (2004).
- [38] S. Kumar and S. Thakur, Local polar and long-range isotropic activity assisted swelling and collapse dynamics of an active ring polymer, *Macromolecules* **56**, 5229 (2023).
- [39] E. F. Teixeira, H. C. M. Fernandes, and L. G. Brunnet, A single active ring model with velocity self-alignment, *Soft Matter* **17**, 5991 (2021).
- [40] L. Theeyancheri, S. Chaki, T. Bhattacharjee, and R. Chakrabarti, Migration of active rings in porous media, *Phys. Rev. E* **106**, 014504 (2022).
- [41] L. Liu, E. Tüzel, and J. L. Ross, Loop formation of microtubules during gliding at high density, *J. Phys.: Condens. Matter* **23**, 374104 (2011).
- [42] T. Sakaue, G. Witz, G. Dietler, and H. Wada, Universal bond correlation function for two-dimensional polymer rings, *EPL* **91**, 68002 (2010).
- [43] F. Drube, K. Alim, G. Witz, G. Dietler, and E. Frey, Excluded volume effects on semiflexible ring polymers, *Nano Lett.* **10**, 1445 (2010).

- [44] M. Ripoll, R. G. Winkler, and G. Gompper, Hydrodynamic screening of star polymers in shear flow, *Eur. Phys. J. E* **23**, 349 (2007).
- [45] R. Kapral, Multiparticle collision dynamics: Simulations of complex systems on mesoscale, *Adv. Chem. Phys.* **140**, 89 (2008).
- [46] G. Gompper, T. Ihle, D. M. Kroll, and R. G. Winkler, Multi-particle collision dynamics: A particle-based mesoscale simulation approach to the hydrodynamics of complex fluids, *Adv. Polym. Sci.* **221**, 1 (2009).
- [47] R. Finken, A. Lamura, U. Seifert, and G. Gompper, Two-dimensional fluctuating vesicles in linear shear flow, *Eur. Phys. J. E* **25**, 309 (2008).
- [48] B. Kaoui, J. Harting, and C. Misbah, Two-dimensional vesicle dynamics under shear flow: Effect of confinement, *Phys. Rev. E* **83**, 066319 (2011).
- [49] A. Lamura, Numerical study of a confined vesicle in shear flow at finite temperature, *Mathematics* **10**, 3570 (2022).
- [50] R. G. Winkler, P. Reineker, and L. Harnau, Models and equilibrium properties of stiff molecular chains, *J. Chem. Phys.* **101**, 8119 (1994).
- [51] V. Bianco, E. Locatelli, and P. Maggaretti, Globulelike conformation and enhanced diffusion of active polymers, *Phys. Rev. Lett.* **121**, 217802 (2018).
- [52] J. P. Miranda-López, E. Locatelli, and C. Valeriani, Self-organized states of solutions of active ring polymers in bulk and under confinement, *J. Chem. Theory Comput.* **20**, 1636 (2024).
- [53] W. C. Swope, H. C. Andersen, P. H. Berens, and K. R. Wilson, A computer simulation method for the calculation of equilibrium constants for the formation of physical clusters of molecules: Application to small water clusters, *J. Chem. Phys.* **76**, 637 (1982).
- [54] M. P. Allen and D. J. Tildesley, *Computer Simulation of Liquids* (Clarendon Press, Oxford, 1987).
- [55] N. Kikuchi, C. M. Pooley, J. F. Ryder, and J. M. Yeomans, Transport coefficients of a mesoscopic fluid dynamics model, *J. Chem. Phys.* **119**, 6388 (2003).
- [56] T. Ihle and D. M. Kroll, Stochastic rotation dynamics: A Galilean-invariant mesoscopic model for fluid flow, *Phys. Rev. E* **63**, 020201(R) (2001).
- [57] A. Lamura, G. Gompper, T. Ihle, and D. M. Kroll, Multiparticle collision dynamics: Flow around a circular and a square cylinder, *Europhys. Lett.* **56**, 319 (2001).
- [58] B. Rupp and F. Nédélec, Patterns of molecular motors that guide and sort filaments, *Lab*

- Chip **12**, 4903 (2012).
- [59] H. W. Diehl and E. Eisenriegler, Universal shape ratios for open and closed random walks: exact results for all d , *J. Phys. A* **22**, L87 (1989).
- [60] A. Nikoubashman, A. Milchev, and K. Binder, Dynamics of single semiflexible polymers in dilute solution, *J. Chem. Phys.* **145**, 234903 (2016).
- [61] E. Farge and A. C. Maggs, Dynamic scattering from semiflexible polymers, *Macromolecules* **26**, 5041 (1993).
- [62] R. G. Winkler, Diffusion and segmental dynamics of rodlike molecules by fluorescence correlation spectroscopy, *J. Chem. Phys.* **127**, 054904 (2007).
- [63] A. Martin-Gomez, G. Gompper, and R. G. Winkler, Active Brownian filamentous polymers under shear flow, *Polymers* **10**, 837 (2018).
- [64] A. Panda, R. G. Winkler, and S. P. Singh, Characteristic features of self-avoiding active Brownian polymers under linear shear flow, *Soft Matter* **19**, 8577 (2023).

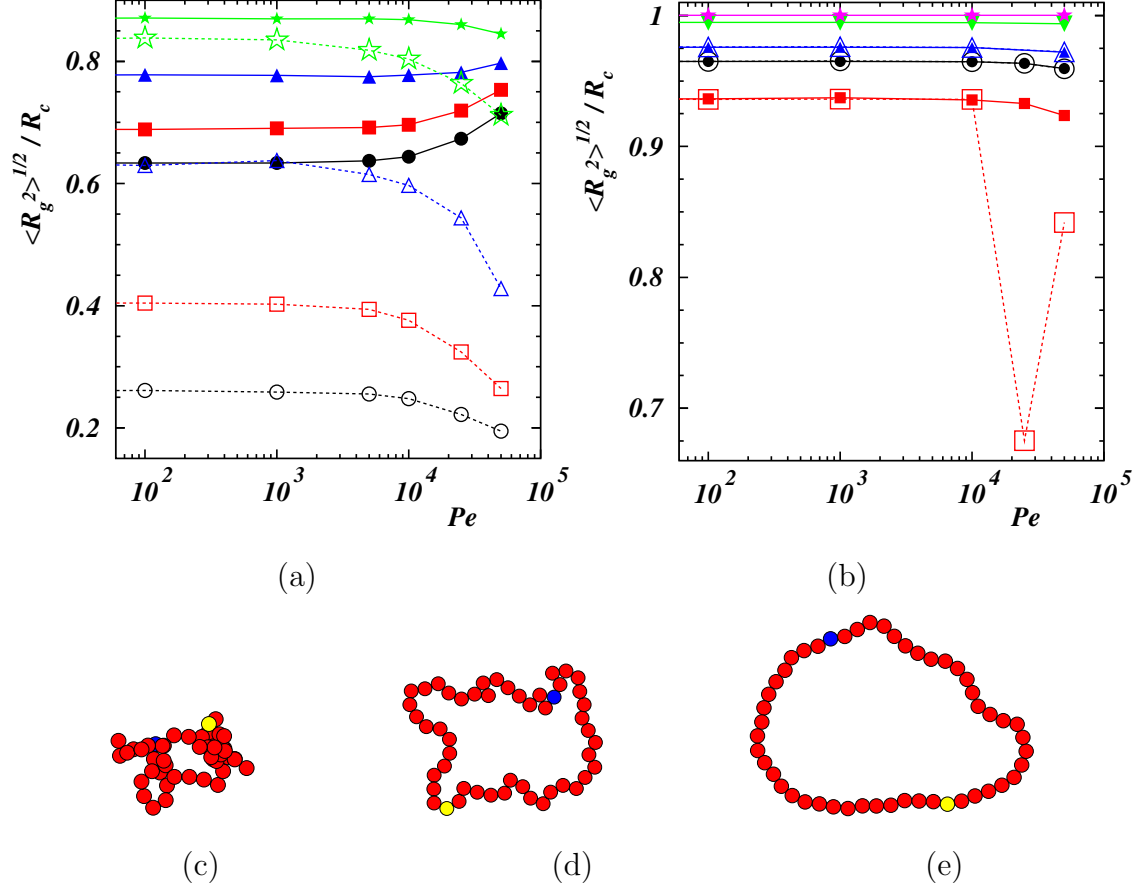


FIG. 1. Root-mean-square values of the radius of gyration R_g as function of the Péclet number Pe in the (a) flexible regime for $L_p/L = 0$ (black circles), 0.04 (red squares), 0.1 (blue up triangles), 0.2 (green stars), and in the (b) stiff regime for $L_p/L = 0.4$ (red squares), 0.7 (black circles), 1 (blue up triangles), 4 (green down triangles), 40 (purple stars). Filled and empty symbols correspond to the SAR and PAR models, respectively. $R_c = L/(2\pi)$ is the radius of the corresponding rigid ring. Typical conformations of rings at $Pe = 2.5 \times 10^4$ for the PAR model with $L_p/L = 0.04$ (c) and the SAR model with $L_p/L = 0.04$ (d), 0.4 (e). The beads 1 and $N/2 + 1$ are colored blue and yellow, respectively.

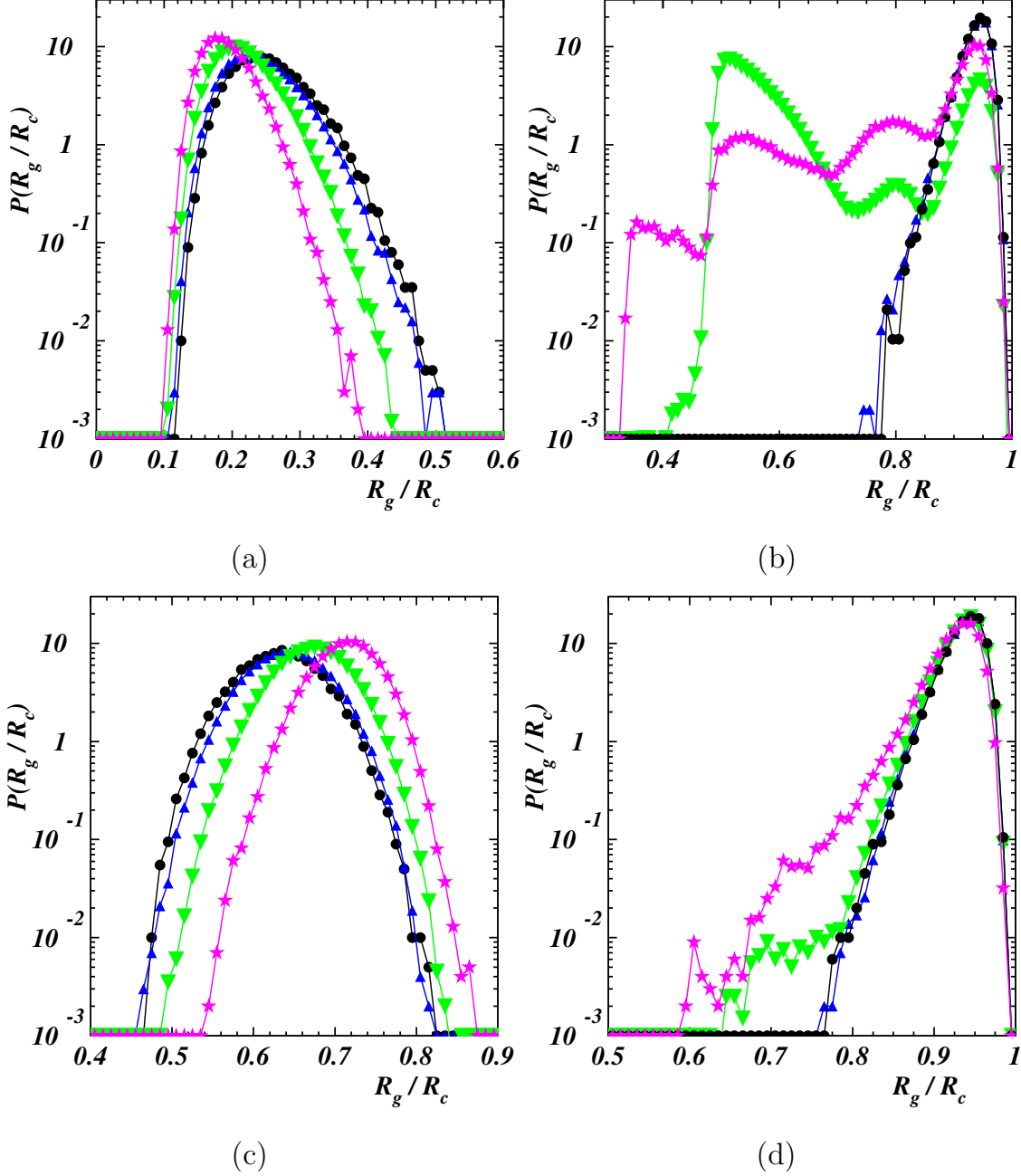


FIG. 2. Normalized probability distribution function of the radius of gyration R_g for PAR (upper row) and SAR (lower row) models with $L_p/L = 0$ (a,c), 0.4 (b,d) and $Pe = 0$ (black circles), 10^4 (blue up triangles), 2.5×10^4 (green down triangles), 5×10^4 (purple stars). $R_c = L/(2\pi)$ is the radius of the corresponding rigid ring.

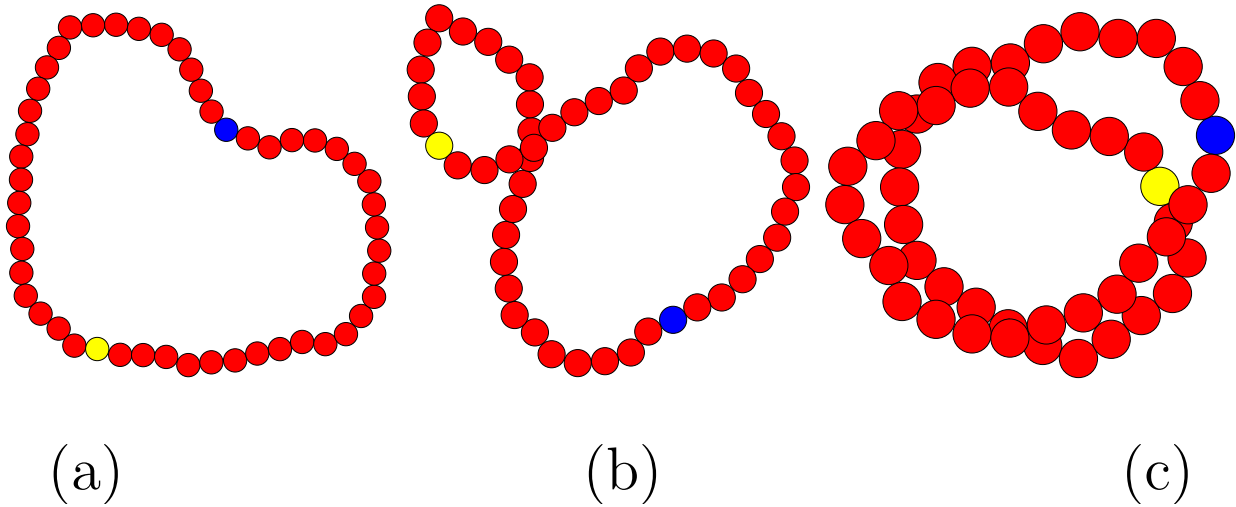


FIG. 3. Typical conformations of a ring with $L_p/L = 0.4$ at $Pe = 2.5 \times 10^4$ for the PAR model corresponding to the positions $R_g/R_c \simeq 0.95$ (a), 0.80 (b), 0.52 (c) of the three peaks of the corresponding probability distribution of Fig. 2 (b). The beads 1 and $N/2 + 1$ are colored blue and yellow, respectively.

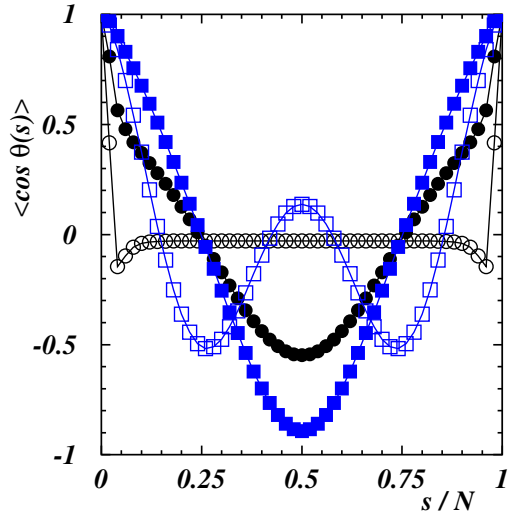


FIG. 4. Bond correlation function versus the scaled contour separation s/N for $Pe = 2.5 \times 10^4$ and $L_p/L = 0$ (black circles), 0.4 (blue squares). Filled and empty symbols correspond to the SAR and PAR models, respectively.

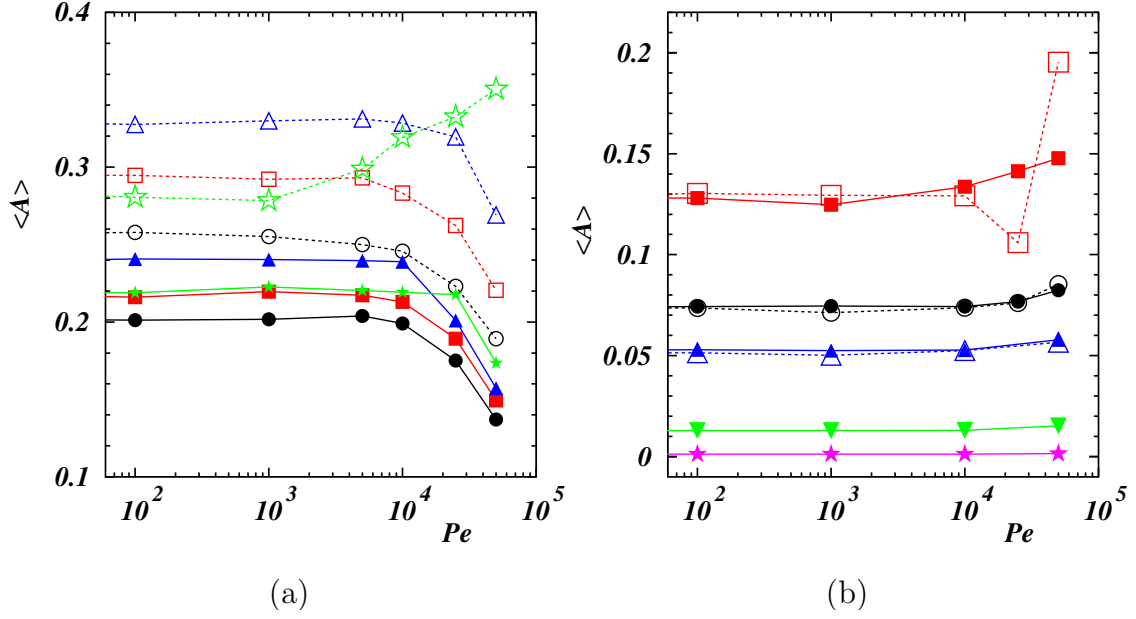


FIG. 5. Average values of the asphericity A as function of the Péclet number Pe in the (a) flexible regime for $L_p/L = 0$ (black circles), 0.04 (red squares), 0.1 (blue up triangles), 0.2 (green stars), and in the (b) stiff regime for $L_p/L = 0.4$ (red squares), 0.7 (black circles), 1 (blue up triangles), 4 (green down triangles), 40 (purple stars). Filled and empty symbols correspond to the SAR and PAR models, respectively.

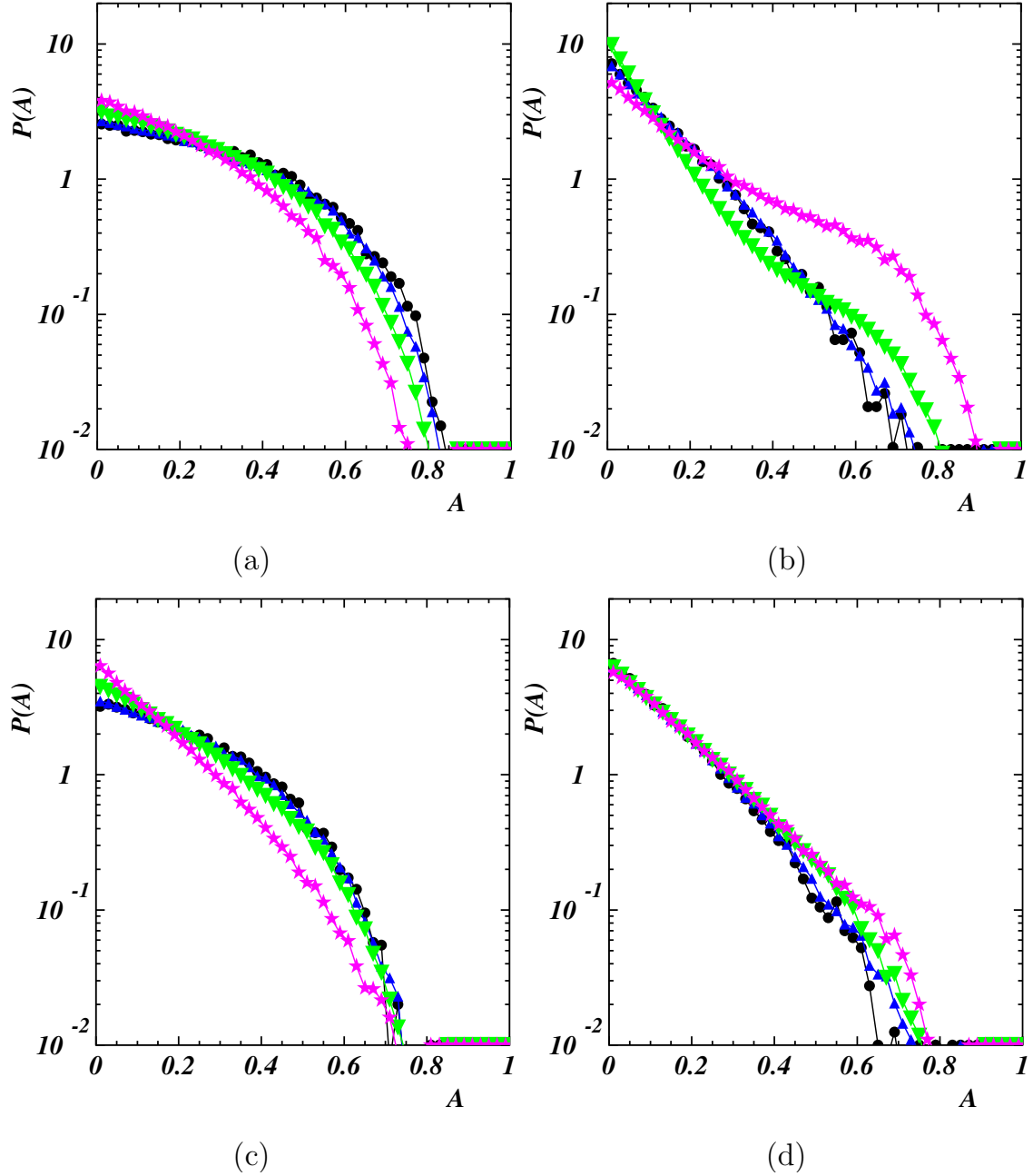


FIG. 6. Normalized probability distribution function of the asphericity A for for PAR (upper row) and SAR (lower row) models with $L_p/L = 0$ (a,c), 0.4 (b,d) and $Pe = 0$ (black circles), 10^4 (blue up triangles), 2.5×10^4 (green down triangles), 5×10^4 (purple stars).

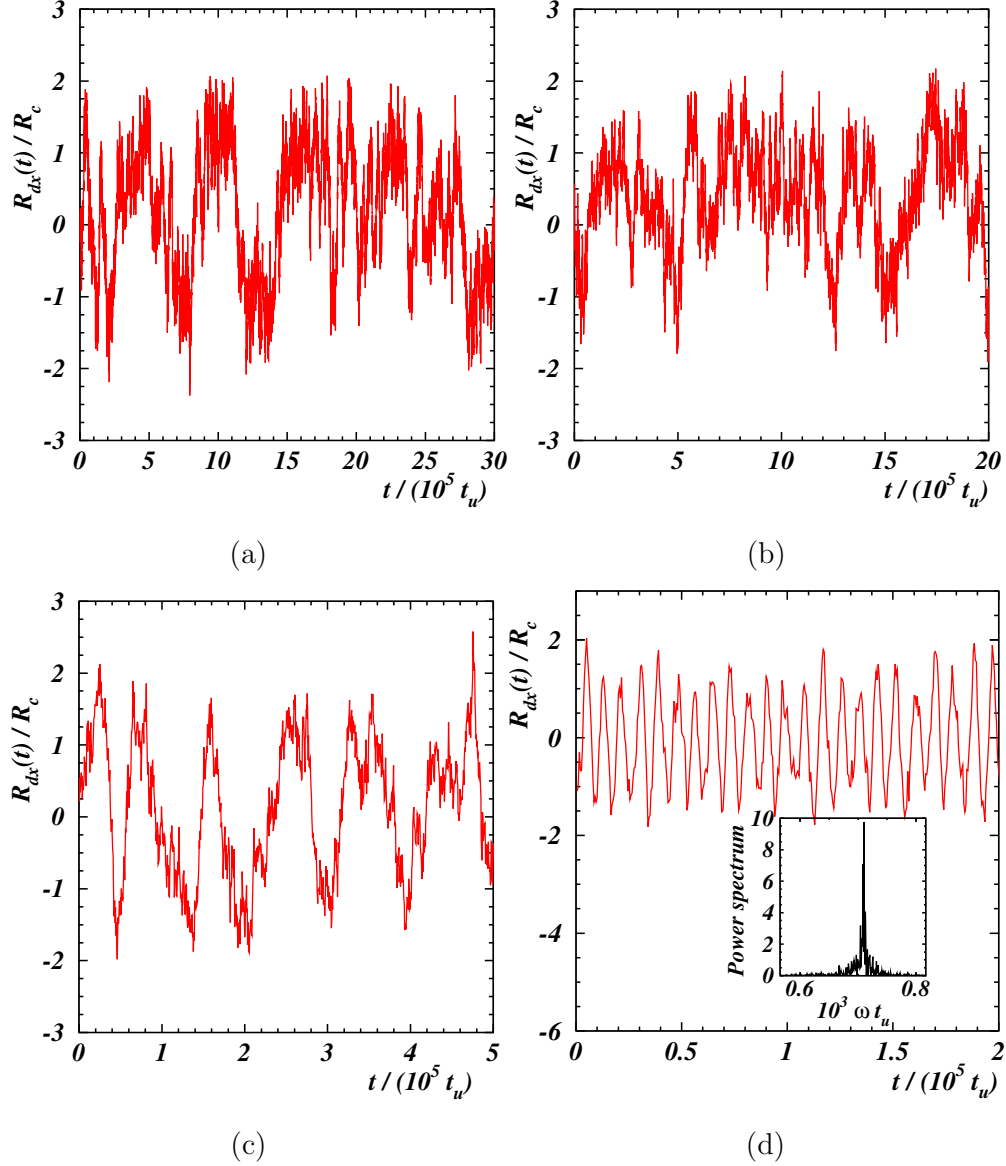


FIG. 7. Time behavior of the x -component R_{dx} of the ring-diameter vector \mathbf{R}_d for the flexible, $L_p/L = 0.04$, self-avoiding ring at $Pe = 0$ (a), 10 (b), 10^2 (c), 10^3 (d). In the inset of panel (d) the corresponding power spectrum (in arbitrary units) is shown as a function of the frequency ω . $R_c = L/(2\pi)$ is the radius of the corresponding rigid ring.

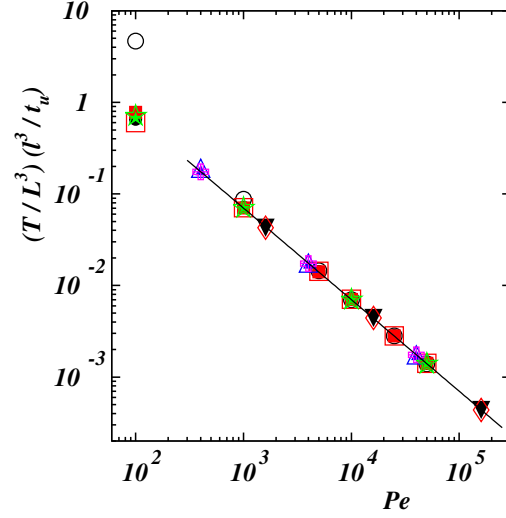


FIG. 8. Period T of the rotational motion of active rings, rescaled by the polymer length L , as function of the Péclet number Pe for $L_p/L = 0$ (black circles), 0.1 (red squares), 1 (green stars) with $L = 50l$, for $L_p/L = 0.1$ (blue triangles up), 1 (purple plus symbols) with $L = 100l$, and for $L_p/L = 0.1$ (red diamonds), 1 (black triangles down) with $L = 200l$. Filled and empty symbols correspond to the SAR and PAR models, respectively. The black line has slope -1 .

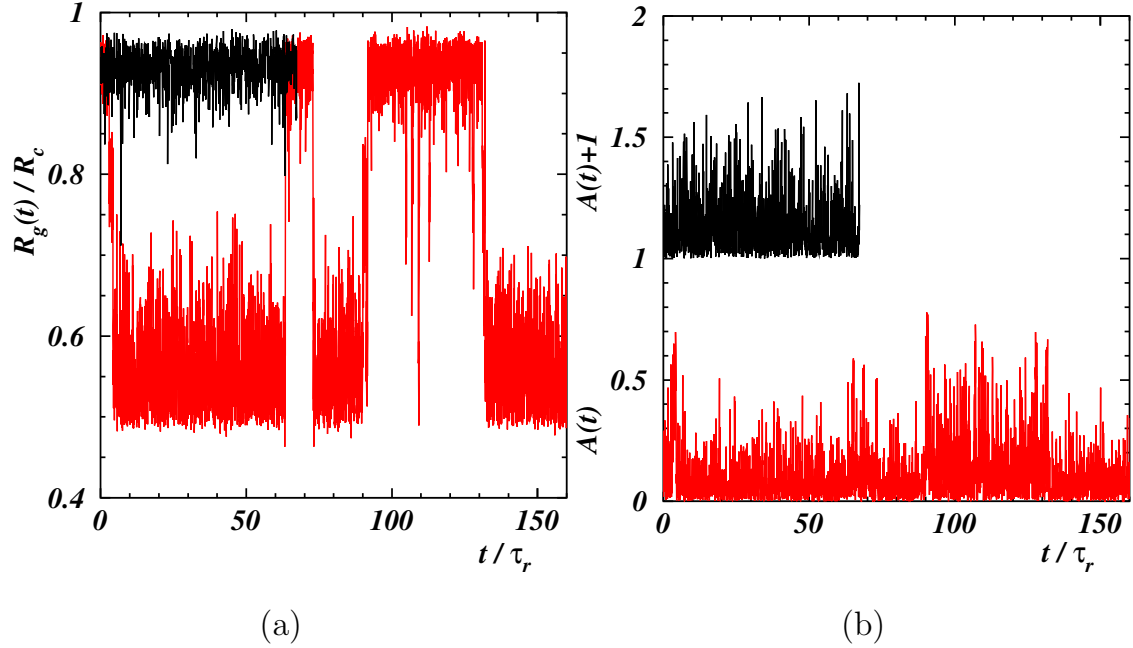


FIG. 9. Radius of gyration R_g (a) and asphericity A (b) as functions of time t/τ_r , where τ_r is the polymer relaxation time, with $L_p/L = 0.4$ at $Pe = 2.5 \times 10^4$ for SAR (black line) and PAR (red line) models. $R_c = L/(2\pi)$ is the radius of the corresponding rigid ring. The asphericity of the SAR model in panel (b) has been shifted by 1 to avoid overlap with the red curve.

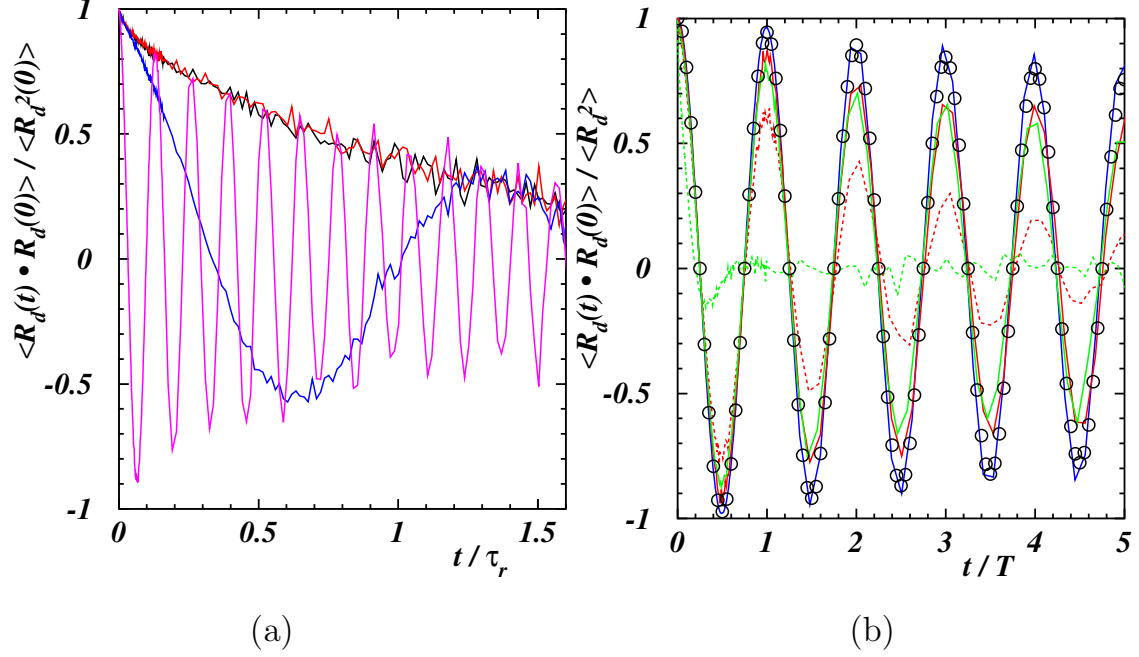


FIG. 10. (a) Autocorrelation function of the ring diameter $\mathbf{R}_d(t)$ as a function of time t/τ_r , where τ_r is the polymer relaxation time, for a self-avoiding active ring with $L_p/L = 0.04$ and $Pe = 0$ (black line), 10 (red line), 10^2 (blue line), 10^3 (purple line). (b) Autocorrelation function of the ring diameter $\mathbf{R}_d(t)$ as a function of time t/T , where T is the computed rotational period, for $Pe = 10^3$ and $L_p/L = 0$ (green line), 0.1 (red line), 40 (blue line). Full and dashed lines correspond to the SAR and PAR models, respectively. The black empty circles correspond to the theoretical prediction (9) [31] when $L_p/L = 40$.

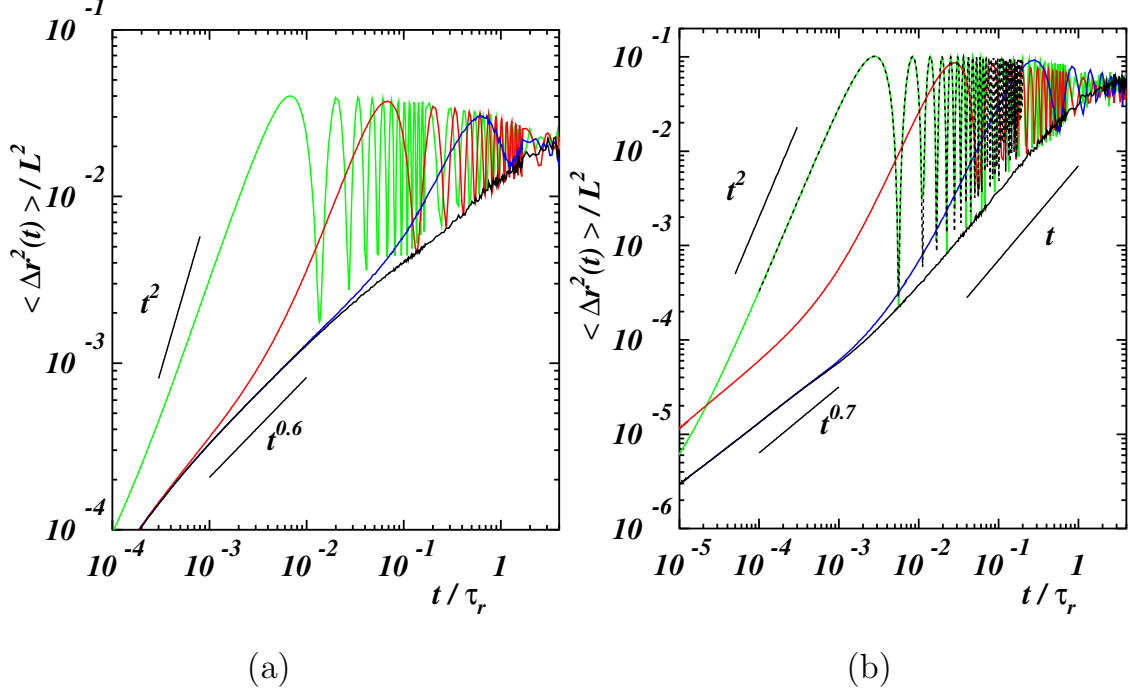


FIG. 11. Beads mean-square displacement relative to the center-of-mass mean-square displacement, $\langle \Delta r^2(t) \rangle$, of self-avoiding (a) flexible, $L_p/L = 0$, and (b) stiff, $L_p/L = 40$, active rings as function of time t/τ_r , where τ_r is the polymer relaxation time, for Péclet numbers $Pe = 0$ (black line), 10^2 (blue line), 10^3 (red line), 10^4 (green line). Short black lines indicate power laws with the annotated time dependence. In panel (b) the black dashed line corresponds to the theoretical prediction (10) [31] when $Pe = 10^4$.